International Journal of Solids and Structures 128 (2017) 296–308

Contents lists available at ScienceDirect

International Journal of Solids and Structures

journal homepage: www.elsevier.com/locate/ijsolstr

Moisture-induced buckling of paper sheets, analysis and simulation

R. de Böck[a,*], A.A.F. van de Ven[a], L.H. Saes[b], J.M.L. Maubach[a], B. Koren[a]

[a] Department of Mathematics and Computer Science, Eindhoven University of Technology, The Netherlands
[b] Océ Technologies B.V., Venlo, The Netherlands

ARTICLE INFO

Article history:
Received 14 March 2017
Revised 17 August 2017
Available online 15 September 2017

Keywords:
Paper deformation
Buckling
von Kármán plate theory
Rayleigh–Ritz method
Nonlinear simulation

ABSTRACT

Understanding the effects of water absorption on the geometry of a paper sheet is important for inkjet printing applications, since internal moisture content differences may cause unacceptable out-of-plane deformations. The present work focuses on moisture-induced deformations due to a moisture content that is uniform over the thickness of the sheet. Large enough in-plane differences will cause the sheet to buckle, leading to a wavy pattern at the edges of the sheet. Two approaches are utilized to study this for levels of moisture content up to and including the threshold for buckling. An analytical approach, based on geometrically nonlinear plate theory (von Kármán theory), and a numerical one, using commercially available finite element software, are presented. As a first reference problem an isotropic circular plate, wetted uniformly at its center, is solved both analytically and numerically for the in-plane stress distribution, the buckling threshold, and the resulting buckling mode. Secondly, the same is done for an orthotropic rectangular plate, wetted at its edges. Here, in the analytical approach a Rayleigh–Ritz analysis is employed to approximate the buckling threshold. The latter is also calculated by numerical means. The results show that the methods provide results consistent with each other.

1. Introduction

Because of its large-scale, worldwide application in printing, paper and its moisture-induced out-of-plane deformations are extensively researched. The phenomena most described in literature are curling, cockling and fluting, see Fig. 1. Leppänen (2007) gives an overview of the literature on this topic. These phenomena mainly result from a through-thickness moisture gradient (Lipponen et al., 2008). The present article focuses on a different type of deformation, induced by an in-plane moisture content gradient. We consider a sheet of paper of which the edges differ from the center with regard to moisture content. This occurs for example when a stack of paper is exposed to a change in ambient humidity. Because of slow diffusion (Marin Zapata, 2010) the edges have a higher moisture content than the center, while a single sheet in the stack has a near-uniform through-thickness moisture content. The gradient of moisture content in the in-plane direction causes the edges to expand, while restricted by the dryer center. When the stresses become large enough, the edges will buckle and form a wavy pattern. The various deformations paper undergoes are depicted in Fig. 1. Apart from the location of the deformation, waviness may appear to be similar to fluting, but these phenomena are fundamentally different; fluting is caused by a through-thickness moisture gradient, the deformation that results is a linear response to this. Waviness is a result of an in-plane moisture gradient, and the non-linear out-of-plane deformation only occurs after buckling.

Whereas the first three phenomena in Fig. 1(a)–(c) have been studied extensively, the last one (d) has not been. However, it is definitely relevant, since in the post-buckling regime the deflections steeply increase with increasing moisture content gradients, resulting in distortions large enough to cause issues in printing.

Classically, buckling is known as a sudden off-line flexure of a beam or a rod under external compression forces (*Euler buckling*). However, in the buckling phenomenon we study here, no external forces are present and the buckling is caused by internal stresses. Comparable kinds of buckling are thermal buckling (Gossard et al., 1952; Giannopoulos et al., 2007; Ma and Wang, 2003), and magneto-elastic buckling (Moon and Pao, 1968; van de Ven, 1978). In all these cases out-of-plane flexure occurs when the internal stresses induced by thermal or electromagnetic fields are large enough. There is a critical magnitude of the gradients in these fields, called the *buckling value*, at which the sheet, in this context commonly referred to as the plate, starts to deflect. Above this threshold we say that the plate is in a *post-buckled* state. The term plate, rather than sheet, is more suited for this context, since in buckling the bending stiffness, no matter how small, becomes relevant.

* Corresponding author.
E-mail addresses: r.d.bock@tue.nl, riendebock@gmail.com (R. de Böck).

http://dx.doi.org/10.1016/j.ijsolstr.2017.08.038
0020-7683/

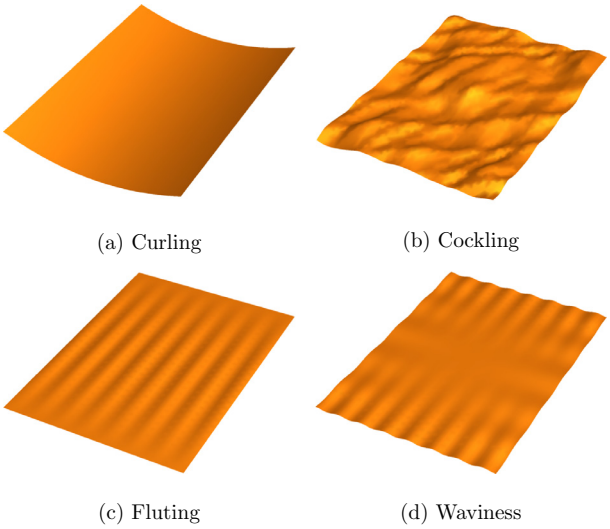

Fig. 1. Schematic representation of the various deformations.

As described in textbooks on the subject matter (Goldmann and Michel, 2001, Ch. 6), (Niskanen, 2012, Ch. 2), the physical properties of paper are difficult to model, because of its complex micro-scale structure. Paper mainly consists of a network of slender wood fibres. Since the thickness of paper sheets is much smaller than the length of the fibres, the network is planar and almost two-dimensional. Due to the manufacturing process the fibres are oriented more in the running direction of the paper machine, commonly referred to as the machine direction (MD), than in the cross direction (CD). This fibre orientation causes differences in physical properties of paper between these two directions: paper is an orthotropic material. One of these differences of great importance to this research is the swelling of paper fibres due to water absorption. At macro-scale paper expands five times more in CD, than in MD.

We consider a single homogeneous sheet of paper, exposed to a uniform rise of moisture content in one part of it, while the remainder maintains its initial moisture content. Apart from this, no external influences are at play. Though diffusion of the moisture content is slow in the case under consideration (Marin Zapata, 2010), it does play a role in reality (Chester and Anand, 2011). We assume that paper exhibits elastic behavior, which, according to Niskanen (2012, Ch. 9), is valid since we consider a one-time wetting with no extreme values for the moisture content. Also, because of its thin shape, with a length-to-thickness ratio of $\mathcal{O}(10^3)$, we approximate it as being two-dimensional, meaning we apply thin-plate theory. Since the deflections of the wavy pattern observed in reality are large, i.e. larger than the thickness of the paper, we employ *von Kármán theory* for thin plates having large deformations. As opposed to linear *Kirchhoff theory*, this formulation admits a geometric nonlinearity, though maintaining constitutive linearity.

Niskanen (2012, Ch. 9) notes that, analogous to linear thermoelasticity, the deformations in a hygrothermoelastic body can be considered as the superposition of an elastic part, obeying Hooke's law, and a part resulting from moisture-induced expansion of paper. Extensive literature on thermal stresses in plates exists. A collection of articles compiled by Hetnarski (2013) offers an overview of the topics related to thermal stresses. This covers a range of subjects applicable to the current work, including thermal buckling of plates, stresses in anisotropic plates and large deflection theory of plates. The boundary conditions, however, are generally taken to be simply supported or clamped, which simplifies calculations. Plates with freely movable boundaries, required for the modeling of waviness in paper, have been researched less. A theoretical framework for the mechanics involved is presented by Efrati et al. (2009). Wavy edges of plant leaves due to growth (Liang and Mahadevan, 2009), as well as torn plastic (Audoly and Boudaoud, 2003) and glass blowing (Sharon and Efrati, 2010) can be described using the same mechanical theory. Klein et al. (2007) perform experiments using circular sheets of a shrinking gel, resulting in an out-of-plane deformation and, in the post-buckling regime, wrinkling. In the context of tissue growth Dervaux et al. (2009) briefly consider wavy edges of paper sheets for comparison. Mead (2003) analyzes an isotropic rectangular plate with free boundaries, subjected to a non-uniform temperature distribution. The author uses a variational method to determine the stresses and applies a Rayleigh–Ritz analysis to determine the buckling threshold and the resulting modes.

A first step towards gaining knowledge of the waviness phenomenon is to study the behavior of the plate up to the onset of buckling, which is the aim of the current work. The buckling threshold is of great importance to this research, since large out-of-plane deformations only occur after the onset of buckling. Moreover, the buckling threshold itself is an important parameter in industrial application of this research, since printing on sheets with large out-of-plane deformations should be avoided.

In the present work we study two reference problems. First, in Section 2 we describe the *von Kármán equations* used to model large deformations of thin plates. In Section 3, we consider an isotropic circular plate, subjected to an increase of moisture content in its center. This problem is tackled using direct methods, by solving the *von Kármán equations* in polar coordinates, which allows for a parameter study. The second reference problem, which is discussed in Section 4, concerns an orthotropic rectangular plate exposed to a rise of moisture content along its edges. The approach outlined by Mead (2003) is generalized to orthotropic *von Kármán equations* and applied to obtain the stresses through variational methods. A Rayleigh–Ritz analysis is applied to approximate the buckling threshold.

The analytical solutions of both reference problems are compared with those obtained through numerical computation, with the commercially available software Marc Mentat (Marc, 2014). We describe the numerical method in Section 5, its results and the comparison with the analytical solutions are discussed in Section 6.

2. Von Kármán equations

Consider a thin rectangular plate of thickness $2h$, with $h/L \ll 1$, where L is some characteristic length for the in-plane dimensions of the plate. We describe the plate by the Cartesian coordinates x, y, z, with x and y the in-plane coordinates and z the coordinate perpendicular to the midplane, $z = 0$. The deformation pattern contains both in-plane and out-of-plane deformations. Let $u = u(x, y)$ and $v = v(x, y)$ represent the midplane displacements in x- and y-direction respectively, and $w = w(x, y)$ the deflection of the midplane in the z-direction. Thus, the total deformation is obtained by superimposing the strains due to stretching and bending of the midplane. For small strains and moderate rotations, the Cartesian components of the deformation tensor are described by the *von Kármán strains* (Ventsel and Krauthammer, 2001, Ch. 7.4):

$$\varepsilon_{xx} = \frac{\partial u}{\partial x} + \frac{1}{2}\left(\frac{\partial w}{\partial x}\right)^2 - z\frac{\partial^2 w}{\partial x^2}, \tag{1a}$$

$$\varepsilon_{xy} = \frac{1}{2}\left(\frac{\partial u}{\partial y} + \frac{\partial v}{\partial x} + \frac{\partial w}{\partial x}\frac{\partial w}{\partial y}\right) - z\frac{\partial^2 w}{\partial x \partial y}, \tag{1b}$$

$$\varepsilon_{yy} = \frac{\partial v}{\partial y} + \frac{1}{2}\left(\frac{\partial w}{\partial y}\right)^2 - z\frac{\partial^2 w}{\partial y^2}. \tag{1c}$$

We consider paper to be an orthotropic medium with fibre orientation running parallel to the x-axis, yielding three mutually orthogonal planes of symmetry in the directions of the Cartesian axes. The total strains in the paper are modeled as a superposition of elastic (Hooke) and hygrothermal deformations, formulated as follows (Lekhnitskii, 1957):

$$\begin{bmatrix}\varepsilon_{xx}\\ \varepsilon_{yy}\\ \varepsilon_{xy}\end{bmatrix} = \begin{bmatrix}\frac{1}{E_x} & -\frac{\nu_{yx}}{E_y} & 0\\ -\frac{\nu_{xy}}{E_x} & \frac{1}{E_y} & 0\\ 0 & 0 & \frac{1}{2G_{xy}}\end{bmatrix}\begin{bmatrix}\sigma_{xx}\\ \sigma_{yy}\\ \sigma_{xy}\end{bmatrix} + \begin{bmatrix}\varepsilon^h_{xx}\\ \varepsilon^h_{yy}\\ 0\end{bmatrix}. \tag{2}$$

Here, E_x, E_y denote the Young's moduli in their respective directions, ν_{xy}, ν_{yx} the Poisson ratios, while G_{xy} is the shear modulus. The stresses corresponding to the von Kármán strains (1) are given by σ_{xx}, σ_{yy}, σ_{xy}. Due to symmetry of the elasticity tensor, $\nu_{xy}/E_x = \nu_{yx}/E_y$. The moisture-induced strains are given by $\varepsilon^h_{xx}(x,y) = \beta_x H(x,y)$ and $\varepsilon^h_{yy}(x,y) = \beta_y H(x,y)$. The z-independent change in moisture content is $H(x, y)$. It is defined as the mass percentage water in the material. The β_i's, $i = x, y$, denote the coefficients of hygro-expansivity, quantifying the relative growth in the respective directions per percent increase of moisture content.

The in-plane stresses $\sigma_{ij}, i, j \in (x, y)$, satisfying the equilibrium equations, are given in terms of the *Airy stress function* as (Ventsel and Krauthammer, 2001, Ch. 7.4)

$$\sigma_{xx} = \frac{\partial^2\varphi}{\partial y^2}, \qquad \sigma_{xy} = -\frac{\partial^2\varphi}{\partial x\partial y}, \qquad \sigma_{yy} = \frac{\partial^2\varphi}{\partial x^2}. \tag{3}$$

To describe the post-buckling state, and to determine the critical buckling value, we need von Kármán's large-deflection equations, which couple the in-plane stress function φ with the out-of-plane deflection w. For these equations, we refer to Lekhnitskii (1957, eq. (7.88)), where they are given for orthotropic plates, however without hygrothermal (or thermal) effects. To incorporate the latter, we have to use (2), after which a derivation analogous to the one in Lekhnitskii (1957) leads us to the following two von Kármán equations:

$$\beta_x\frac{\partial^2 H}{\partial y^2} + \beta_y\frac{\partial^2 H}{\partial x^2} + \frac{1}{E_y}\frac{\partial^4\varphi}{\partial x^4} + \left(\frac{1}{G_{xy}} - 2\frac{\nu_{xy}}{E_x}\right)\frac{\partial^4\varphi}{\partial x^2\partial y^2} + \frac{1}{E_x}\frac{\partial^4\varphi}{\partial y^4} = \left(\frac{\partial^2 w}{\partial x\partial y}\right)^2 - \frac{\partial^2 w}{\partial x^2}\frac{\partial^2 w}{\partial y^2}, \tag{4}$$

and

$$\frac{2h^3}{3}\left(\frac{E_x}{1-\nu_{xy}\nu_{yx}}\frac{\partial^4 w}{\partial x^4} + 2\left(\frac{\nu_{yx}E_x}{1-\nu_{xy}\nu_{yx}} + 2G_{xy}\right)\frac{\partial^4 w}{\partial x^2\partial y^2} + \frac{E_y}{1-\nu_{xy}\nu_{yx}}\frac{\partial^4 w}{\partial y^4}\right) = 2h\left(\frac{\partial^2\varphi}{\partial x^2}\frac{\partial^2 w}{\partial y^2} + \frac{\partial^2\varphi}{\partial y^2}\frac{\partial^2 w}{\partial x^2} - 2\frac{\partial^2\varphi}{\partial x\partial y}\frac{\partial^2 w}{\partial x\partial y}\right). \tag{5}$$

For the determination of the buckling value, we first need to know the pre-buckled state, i.e. the state in which the plate does not deflect, but deforms in its plane only. The only unknown is then the Airy stress function $\varphi(x, y)$, governed by the bi-harmonic equation that follows from (4) with $w(x, y) = 0$,

$$\beta_x\frac{\partial^2 H}{\partial y^2} + \beta_y\frac{\partial^2 H}{\partial x^2} + \frac{1}{E_y}\frac{\partial^4\varphi}{\partial x^4} + \left(\frac{1}{G_{xy}} - 2\frac{\nu_{xy}}{E_x}\right)\frac{\partial^4\varphi}{\partial x^2\partial y^2} + \frac{1}{E_x}\frac{\partial^4\varphi}{\partial y^4} = 0. \tag{6}$$

To obtain the buckling value, we first solve (6) under the appropriate boundary conditions (to be discussed further on) yielding φ as a function of H. Substituting this φ into (5), we obtain a homogeneous equation for w. Since for a free plate the boundary conditions are uniform, the trivial initial state $w \equiv 0$ is always a solution for this problem. Only when the derivatives of H are of a critical threshold magnitude, non-zero solutions for w are possible. This critical threshold is the buckling value. It should be noted here that in our applications we always assume a piece-wise uniform H, i.e. either $H(x, y) = 0$, or $H(x, y) = \chi$, for some value χ. This means the derivatives of H are not defined at the discontinuities, but since we will use the variational formulation to obtain solutions in the following, this will not pose a problem. For loads beyond the buckling load, the plate is in the post-buckling state, in which the deflections of the plate become dominant. To describe this state, we need the full coupled set (4) and (5). We use the finite element software Marc Mentat (Marc, 2014) to solve this problem numerically.

In the sequel we prefer to work with a dimensionless version of the von Kármán equations. To this end, we introduce the following dimensionless coordinates and variables:

$$\hat{x} = \frac{x}{L}, \quad \hat{y} = \frac{y}{L}, \quad \hat{H} = \frac{H}{\chi}, \quad \hat{w} = \frac{w}{W}, \quad \hat{\varphi} = \frac{\varphi}{\Phi}, \quad \hat{\varepsilon}^h_{xx(yy)} = \frac{\varepsilon^h_{xx(yy)}}{\varepsilon_0}, \tag{7}$$

where, with χ the maximum of $H(x, y)$,

$$W = \sqrt{\varepsilon_0}\,L, \quad \Phi = \varepsilon_0 E_x L^2, \quad \varepsilon_0 = \beta_x\chi. \tag{8}$$

Substituting these dimensionless quantities into the von Kármán equations (4) and (5) we obtain, upon omitting the hats:

$$\frac{\partial^2 H}{\partial y^2} + \beta\frac{\partial^2 H}{\partial x^2} + \tilde{E}\frac{\partial^4\varphi}{\partial x^4} + 2\gamma^2\frac{\partial^4\varphi}{\partial x^2\partial y^2} + \frac{\partial^4\varphi}{\partial y^4} = \left(\frac{\partial^2 w}{\partial x\partial y}\right)^2 - \frac{\partial^2 w}{\partial x^2}\frac{\partial^2 w}{\partial y^2}, \tag{9}$$

and

$$\frac{\partial^4 w}{\partial x^4} + 2\Gamma\frac{\partial^4 w}{\partial x^2\partial y^2} + \frac{1}{\tilde{E}}\frac{\partial^4 w}{\partial y^4} = \mu\left(\frac{\partial^2\varphi}{\partial x^2}\frac{\partial^2 w}{\partial y^2} + \frac{\partial^2\varphi}{\partial y^2}\frac{\partial^2 w}{\partial x^2} - 2\frac{\partial^2\varphi}{\partial x\partial y}\frac{\partial^2 w}{\partial x\partial y}\right), \tag{10}$$

with

$$\beta = \frac{\beta_y}{\beta_x}, \quad \tilde{E} = \frac{E_x}{E_y}, \quad \gamma = \sqrt{\frac{E_x}{2G_{xy}} - \nu_{xy}}, \tag{11}$$

and

$$\Gamma = \nu_{yx} + 2\frac{(1-\nu_{xy}\nu_{yx})G_{xy}}{E_x}, \quad \mu = 3(1-\nu_{xy}\nu_{yx})\beta_x\chi\frac{L^2}{h^2}. \tag{12}$$

Since $\varepsilon_0 = \beta_x\chi$ is a measure for the in-plane strains induced by the wetting of the paper, the dimensionless parameter ε_0 is small. If $\varepsilon_0 = \mathcal{O}(h^2/L^2) \ll 1$, then $\mu = \mathcal{O}(1)$. Notice that as this parameter is characteristic for wetting, it determines the onset of buckling of the paper. Hence, the critical value of μ represents the buckling value we are looking for.

3. Circular plate

As a first reference problem, we consider an isotropic circular plate of thickness $2h$ and radius R, with radial coordinate r. The edge of the plate at $r = R$ is free. An inner circle with radius a located at the center, is uniformly moistened, while the remainder of the plate maintains its initial moisture content. This input parameter a is in general an unknown, which is to be determined through a diffusion-deformation study, see e.g. Chester and Anand (2011). The slow diffusion of moisture in paper (Marin Zapata, 2010) justifies the choice to regard this parameter as a constant in this study.

We non-dimensionalize the radii by dividing by R and drop the hats. The problem is axisymmetric. Hence,

$$H(x,y) = H(r) = \begin{cases} \chi, & 0 \le r < a, \\ 0, & a < r \le 1. \end{cases} \tag{13}$$

We start with the in-plane problem governed by the biharmonic equation for the stress function (6). In this case, $\varphi = \varphi(r)$ and it can be replaced by an alternative stress function $\psi(r) = \varphi'(r)$, for which the formulas for the two remaining stresses become

$$\sigma_{rr} = \frac{\psi(r)}{r}, \quad \sigma_{\theta\theta} = \psi'(r). \tag{14}$$

This stress function is the solution of the axisymmetric version of (6). For the dimensionless version we will use here (9) with $w = 0$ and $\tilde{E} = \gamma = 1$, reading:

$$\psi''(r) + \frac{\psi'(r)}{r} - \frac{\psi(r)}{r^2} = -\beta H'(r) = 0, \qquad \text{for} \quad r \neq a, \tag{15}$$

which is the in-plane part of the *von Kármán equations* in polar coordinates. Since the moisture content is piece-wise constant, $H'(r) = 0$ for every r except $r = a$. Hence, the effect of the discontinuous moisture content turns up only in the jump conditions at $r = a$.

Solving this equation in the regions $0 \le r < a$ and $a < r \le 1$, and accounting for the continuity of the displacement and the stress σ_{rr} across $r = a$, we find by standard calculations, for the dimensionless stress function $\psi = \hat{\psi} = \psi/\Psi$, $\Psi = \chi\beta ER$,

$$\psi(r) = \begin{cases} -\frac{1}{2}(1-a^2)r\,, & 0 \le r < a, \\ -\frac{1}{2}\left(\frac{1}{r} - r\right), & a < r \le 1. \end{cases} \tag{16}$$

The stresses are found using (14) (now in dimensional form):

$$\sigma_{rr}(r) = \begin{cases} \dfrac{(a^2-R^2)E\beta\chi}{2R^2}\,, & 0 \le r < a, \\ \dfrac{a^2E\beta\chi}{2R^2}\left(1 - \dfrac{R^2}{r^2}\right), & a < r \le R, \end{cases} \tag{17}$$

$$\sigma_{\theta\theta}(r) = \begin{cases} \dfrac{(a^2-R^2)E\beta\chi}{2R^2}\,, & 0 \le r < a, \\ \dfrac{a^2E\beta\chi}{2R^2}\left(1 + \dfrac{R^2}{r^2}\right), & a < r \le R. \end{cases} \tag{18}$$

We note that the stresses are uniform in the inner part. Next we consider the out-of-plane part of the *von Kármán equations* (10) in terms of the stress function we just obtained and in a reduced axisymmetric version, reading

$$\Delta^2 w(r) = \mu\Big(\psi(r)w''(r) + \psi'(r)w'(r)\Big), \tag{19}$$

where now $\mu = 3(1-\nu^2)\beta\chi R^2/h^2$. We are looking for the minimal value of μ, or more directly for the moisture content χ, for which (19), under free-boundary conditions, has a non-zero solution for w. This minimum value, μ_0 or χ_0 is the buckling threshold.

We introduce $W(r) := w'(r)$ and integrate (19) to obtain

$$W''(r) + \frac{W'(r)}{r} - \frac{W(r)}{r^2} = \mu\frac{\psi(r)}{r}W(r). \tag{20}$$

We call $W(r) = W_1(r)$ for $0 \le r < a$ and $W(r) = W_2(r)$ for $a < r \le 1$.

First, for $0 \le r < a$, we have

$$W_1''(r) + \frac{W_1'(r)}{r} + \left(A^2 - \frac{1}{r^2}\right)W_1(r) = 0, \tag{21}$$

with

$$A^2 = \frac{1}{2}(1-a^2)\mu. \tag{22}$$

We note that A is real-valued, since all parameters attain positive values, and $a < 1$. In (21) we recognize Bessel's equation, the solutions of which are superpositions of Bessel functions:

$$W_1(r) = C_1J_1(Ar) + \tilde{C}_1Y_1(Ar). \tag{23}$$

Here, J_ν and Y_ν are Bessel functions of the first and second kind, respectively, of degree ν (Abramowitz and Stegun, 1972). Since W_1 must be finite at the center of the circle, $\tilde{C}_1 = 0$.

For $a < r \le 1$, (20) becomes

$$W_2''(r) + \frac{W_2'(r)}{r} + \left(B^2 - \frac{C^2}{r^2}\right)W_2(r) = 0, \tag{24}$$

with

$$B^2 = -\frac{1}{2}\mu a^2, \quad C^2 = 1 - \frac{1}{2}\mu a^2. \tag{25}$$

The general solution of (24) is

$$W_2 = C_2J_C(Br) + C_3Y_C(Br). \tag{26}$$

This solution is also valid with complex values for B and C. The solution to (20) is now given by (23) and (26) as

$$W(r) = \begin{cases} C_1J_1(Ar), & 0 \le r < a, \\ C_2J_C(Br) + C_3Y_C(Br), & a < r \le 1. \end{cases} \tag{27}$$

The continuity and boundary conditions are:

- Continuity of W at $r = a$:

  $W_1(a) = W_2(a)$.
- Continuity of the bending moment at $r = a$:

  $W_1'(a) + \nu W_1(a) = W_2'(a) + \nu W_2(a)$.
- Zero bending moment at the edge $r = 1$:

  $W_2'(1) + \nu W_2(1) = 0$.

These conditions result in a homogeneous system of equations for the coefficient vector $\boldsymbol{C} = \{C_1, C_2, C_3\}^T$:

$$\mathbb{C}\,\boldsymbol{C} = 0, \tag{28}$$

with

$$\mathbb{C} = \begin{bmatrix} J_1(Aa) & -J_C(Ba) & -Y_C(Ba) \\ \frac{A}{B}\Big(J_0(Aa) - J_2(Aa)\Big) & J_{C+1}(Ba) - J_{C-1}(Ba) & Y_{C+1}(Ba) - Y_{C-1}(Ba) \\ 0 & \mathbb{C}_{32} & \mathbb{C}_{33} \end{bmatrix},$$

with

$$\mathbb{C}_{32} = \frac{B}{2}\Big(J_{C-1}(B) - J_{C+1}(B)\Big) + \nu J_C(B),$$

and

$$\mathbb{C}_{33} = \frac{B}{2}\Big(Y_{C-1}(B) - Y_{C+1}(B)\Big) + \nu Y_C(B).$$

This system has a nontrivial solution if and only if the determinant of $\mathbb{C}$ is zero. We are interested in the smallest value for χ for which a nontrivial solution exists, this smallest eigenvalue is the buckling threshold χ_0.

In Section 6, we shall present numerical results obtained through this method, and compare these with the values calculated using Marc Mentat.

4. Rectangular plate

4.1. The in-plane stress function

As a second example, we consider a rectangular plate with length $a, 0 \le x \le a$, width $b, 0 \le y \le b$, and thickness $2h$, $-h \le z \le h$. We introduce the dimensionless in-plane coordinate system

$(\xi, \eta) = (x/a, y/b)$ such that the surface of the plate occupies the space $\mathcal{G} = \{\xi, \eta |\ 0 \le \xi \le 1, 0 \le \eta \le 1\}$. Here, we choose the characteristic length $L = \sqrt{ab}$. A region $\mathcal{G}_1$ is exposed to a uniform rise in moisture content χ, while the remainder of the plate, $\mathcal{G}_2$, maintains its initial moisture content. We define $H(\xi, \eta) := I_{(\xi,\eta)\in\mathcal{G}_1}$, the identity function representing the wet region. We recall that H has been normalized in (7). Taking $w = 0$ in (9) we then obtain here the following bi-harmonic equation for the dimensionless stress function $\varphi(\xi, \eta)$ as

$$\tilde{E}\left(\frac{b}{a}\right)^2 \frac{\partial^4\varphi}{\partial\xi^4} + 2\gamma^2 \frac{\partial^4\varphi}{\partial\xi^2\partial\eta^2} + \left(\frac{a}{b}\right)^2 \frac{\partial^4\varphi}{\partial\eta^4} = -\left(\frac{b}{a}\frac{\partial^2 H}{\partial\xi^2} + \frac{a}{b}\beta\frac{\partial^2 H}{\partial\eta^2}\right). \tag{29}$$

We note that the derivatives of t are not defined at the discontinuities, but since we will use the variational formulation of (29) in the following, we will obtain the relevant terms through partial integration.

The edges of the plate are free, implying that at $\xi = 0, 1$, the stresses σ_{xx} and σ_{xy} must be zero, and likewise at $\eta = 0, 1$, $\sigma_{xy} = \sigma_{yy} = 0$. Using (3) we see that these conditions are satisfied with the following boundary conditions for $\varphi(\xi, \eta)$:

$$\varphi(0,\eta) = \frac{\partial\varphi}{\partial\xi}(0,\eta) = \varphi(1,\eta) = \frac{\partial\varphi}{\partial\xi}(1,\eta) = 0, \tag{30}$$

and

$$\varphi(\xi,0) = \frac{\partial\varphi}{\partial\eta}(\xi,0) = \varphi(\xi,1) = \frac{\partial\varphi}{\partial\eta}(\xi,1) = 0. \tag{31}$$

Following Mead, we choose for $\varphi(\xi, \eta)$ (Mead, 2003, eq.(A.3)):

$$\varphi(\xi,\eta) = \sum_{m=1}^{M}\sum_{n=1}^{N} A_{mn} f_m(\xi) f_n(\eta), \tag{32}$$

with

$$f_i(\xi) = \cosh(\lambda_i\xi) - \cos(\lambda_i\xi) - \frac{\cosh(\lambda_i) - \cos(\lambda_i)}{\sinh(\lambda_i) - \sin(\lambda_i)}\Big(\sinh(\lambda_i\xi) - \sin(\lambda_i\xi)\Big). \tag{33}$$

These are the modes of a 1-D beam clamped at both edges. For odd-numbered i these functions are symmetric around $\xi = 1/2$, for even values of i they are antisymmetric. The functions satisfy $f_i(0) = f_i(1) = f_i'(0) = 0$, while $f_i'(1) = 0$ leads to the characteristic equation for λ_i:

$$\cosh(\lambda_i)\cos(\lambda_i) = 1. \tag{34}$$

Using these functions the boundary conditions for the stresses are automatically satisfied.

We note that for high i these eigenvalues behave as $\lambda_i \approx (2i + 1)\pi/2$. To circumvent numerical problems for high values of i, we use an adapted formulation for f_i, (Mead, 2003, eq. (A.5)).

After substitution of (32) into (29), we obtain a set of $M \times N$ linear equations for A_{mn} by multiplying (29) with $f_r(\xi)f_s(\eta)$, for $r = 1, 2, \ldots, N$ and $s = 1, 2, \ldots, M$, and integrating the obtained equations over the surface of the plate. Due to the orthogonality of f_i this process yields

$$\mathcal{C} : \mathbb{A} = \mathbb{R}, \tag{35}$$

where $\mathbb{A}$ is the $M \times N$ matrix of the coefficients A_{mn}, and $\mathcal{C}$ a 4-tensor of $\mathcal{O}(M^2N^2)$. Using $\int_0^1 f_k^2(x)\mathrm{d}x = 1,\ \forall k$, we find that its elements are given by

$$\mathcal{C}_{mnmn} = 2\gamma^2 \int_0^1 \big(f_m'(\xi)\big)^2 \mathrm{d}\xi \int_0^1 \big(f_n'(\eta)\big)^2 \mathrm{d}\eta + \lambda_m^4 \tilde{E}\left(\frac{b}{a}\right)^2 + \lambda_n^4\left(\frac{a}{b}\right)^2, \tag{36}$$

for diagonal elements and by

$$\mathcal{C}_{rsmn} = 2\gamma^2 \int_0^1 f_r'(\xi) f_m'(\xi)\mathrm{d}\xi \int_0^1 f_s'(\eta) f_n'(\eta)\mathrm{d}\eta, \tag{37}$$

for off-diagonal terms. The right-hand side $\mathbb{R}$ is an $M \times N$ matrix, of which the elements are given by

$$R_{mn} = -\int_0^1\int_0^1 \left(\frac{a}{b} f_m''(\xi) f_n(\eta) + \beta\frac{b}{a} f_m(\xi) f_n''(\eta)\right) H(\xi,\eta)\mathrm{d}\xi\,\mathrm{d}\eta. \tag{38}$$

Upon solving (35), we obtain the A_{mn}'s and, from (32), a representation for $\varphi(\xi, \eta)$. This method will be applied in Section 6 to specific cases.

4.2. Rayleigh–Ritz method

We proceed with a Rayleigh–Ritz method to obtain an approximation, more specifically an upper bound, for the buckling threshold. This method will be based on the second von Kármán equation (10), which, rewritten in the coordinates ξ and η, becomes here

$$\left(\frac{b}{a}\right)^2 \frac{\partial^4 w}{\partial\xi^4} + 2\Gamma\frac{\partial^4 w}{\partial\xi^2\partial\eta^2} + \frac{1}{\tilde{E}}\left(\frac{a}{b}\right)^2 \frac{\partial^4 w}{\partial\eta^4} = \mu\left(\frac{\partial^2\varphi}{\partial\xi^2}\frac{\partial^2 w}{\partial\eta^2} + \frac{\partial^2\varphi}{\partial\eta^2}\frac{\partial^2 w}{\partial\xi^2} - 2\frac{\partial^2\varphi}{\partial\xi\partial\eta}\frac{\partial^2 w}{\partial\xi\partial\eta}\right). \tag{39}$$

Into this equation the solution for φ obtained in the preceding section is substituted. From this equation we derive expressions for the potential or strain energy U_b due to bending (w) and for the strain energy U_φ due to the in-plane stresses (φ). The *Rayleigh–Ritz principle* then states that the buckling value is equal to the minimum of the quotient of U_b and U_φ over the set of all kinematically admissible displacements w. However, since this set needs to satisfy kinematic boundary conditions only and since the edges of the plate are free (only dynamic boundary conditions), we have no restrictions with respect to boundary conditions when choosing an admissible deflection field $w(\xi, \eta)$. For w we choose the representation

$$w(\xi,\eta) = \sum_{i=1}^{I}\sum_{j=1}^{J} W_{ij} g_i(\xi) g_j(\eta). \tag{40}$$

The functions g_i need to be linearly independent and they should be chosen such that they span all possible deflection patterns.

The out-of-plane part of the strain energy due to bending U_b is found from (39) by multiplying the left-hand side of this equation by w and then integrating it over the surface of the plate. After some integrations by part, in which the homogeneous boundary conditions are used, this leads us to the expression for the strain energy due to bending (scaled, dimensionless), compare with Mead (2003, eq. (7));

$$U_b = \int_0^1\int_0^1 \left(\left(\frac{b}{a}\right)^2\left(\frac{\partial^2 w}{\partial\xi^2}\right)^2 + 2\Gamma_1\frac{\partial^2 w}{\partial\xi^2}\frac{\partial^2 w}{\partial\eta^2} + \tilde{E}\left(\frac{a}{b}\right)^2\left(\frac{\partial^2 w}{\partial\eta^2}\right)^2 + 2\Gamma_2\left(\frac{\partial^2 w}{\partial\xi\,\partial\eta}\right)^2\right)\mathrm{d}\xi\,\mathrm{d}\eta, \tag{41}$$

with

$$\Gamma_1 = \nu_{yx}, \qquad \Gamma_2 = \frac{G_{xy}}{E_x}\,(1 - \nu_{xy}\nu_{yx}). \tag{42}$$

In a more or less analogous way the work done by in-plane stresses U_φ is here obtained by multiplying the right-hand side of (39) by w, integrating over the surface of the plate and applying

two integrations by part, yielding

$$U_\varphi = \int_0^1 \int_0^1 \left(\frac{\partial^2 \varphi}{\partial \eta^2} \left(\frac{\partial w}{\partial \xi} \right)^2 + \frac{\partial^2 \varphi}{\partial \xi^2} \left(\frac{\partial w}{\partial \eta} \right)^2 - 2 \frac{\partial^2 \varphi}{\partial \xi \partial \eta} \frac{\partial w}{\partial \xi} \frac{\partial w}{\partial \eta} \right) \mathrm{d}\xi \, \mathrm{d}\eta. \tag{43}$$

This energy is entirely due to the increase of moisture content and can therefore also be called *hygro-elastic energy*.

In a Rayleigh–Ritz procedure the buckling value for the moisture content, represented here by the dimensionless parameter μ, is found as the minimum of the Rayleigh quotient U_b/U_φ over the whole set $\{W_{kl}\}$. This means that the buckling value μ_0 is found by solving the eigensystem

$$\frac{\partial U_b}{\partial W_{kl}} - \mu \frac{\partial U_\varphi}{\partial W_{kl}} = 0, \tag{44}$$

for μ. In practice we restrict ourselves to a finite set of coefficients W_{kl}.

After substitution of (42) we differentiate successively (41) and (43) with respect to W_{kl} to obtain:

$$\begin{aligned} \frac{\partial U_b}{\partial W_{kl}} = \sum_{i=1}^{I} \sum_{j=1}^{J} W_{ij} \int_0^1 \int_0^1 \Bigg(& \left(\frac{b}{a} \right)^2 g_k''(\xi) g_i''(\xi) g_l(\eta) g_j(\eta) \\ & + \Gamma_1 \left(g_k''(\xi) g_i(\xi) g_l(\eta) g_j''(\eta) + g_k(\xi) g_i''(\xi) g_l''(\eta) g_j(\eta) \right) \\ & + \frac{1}{\tilde{E}} \left(\frac{a}{b} \right)^2 g_k(\xi) g_i(\xi) g_l''(\eta) g_j''(\eta) + 2\Gamma_2 g_k'(\xi) g_i'(\xi) g_l'(\eta) g_j'(\eta) \Bigg) \\ & \mathrm{d}\xi \, \mathrm{d}\eta. \end{aligned} \tag{45}$$

and

$$\frac{\partial U_\varphi}{\partial W_{kl}} = -\sum_{i=1}^{I} \sum_{j=1}^{J} \sum_{m=1}^{M} \sum_{n=1}^{N} W_{ij} A_{mn} \left(I_{1,klmn} - I_{2,klmn} - I_{3,klmn} + I_{4,klmn} \right), \tag{46}$$

with

$$I_{1,klmn} = \int_0^1 \int_0^1 \left(f_m(\xi) g_i'(\xi) g_k'(\xi) f_n''(\eta) g_j(\eta) g_l(\eta) \right) \mathrm{d}\xi \, \mathrm{d}\eta, \tag{47a}$$

$$I_{2,klmn} = \int_0^1 \int_0^1 \left(f_m'(\xi) g_i'(\xi) g_k(\xi) f_n'(\eta) g_j(\eta) g_l'(\eta) \right) \mathrm{d}\xi \, \mathrm{d}\eta, \tag{47b}$$

$$I_{3,klmn} = \int_0^1 \int_0^1 \left(f_m'(\xi) g_i(\xi) g_k'(\xi) f_n'(\eta) g_j'(\eta) g_l(\eta) \right) \mathrm{d}\xi \, \mathrm{d}\eta, \tag{47c}$$

$$I_{4,klmn} = \int_0^1 \int_0^1 \left(f_m''(\xi) g_i(\xi) g_k(\xi) f_n(\eta) g_j'(\eta) g_l'(\eta) \right) \mathrm{d}\xi \, \mathrm{d}\eta. \tag{47d}$$

5. Numerical approach

Besides the previous analytical solution approaches we also consider a numerical approach. For this Marc Mentat (Marc, 2014) is used. It is especially suited to deal with nonlinear problems. The rectangular plate is subdivided into rectangles by partitioning it uniformly. For the circular plate polar coordinates are used. The radius and the angle are subdivided and edges of elements are linearized. In the wetted region a finer grid will be used to better capture the stress distribution.

The simulations are performed using bilinear thick-shell elements. The thick-shell property of these elements indicates that their formulation is based on von Kármán theory, which makes them suitable for nonlinearities due to large deformations.

The boundary conditions at the edges of the plate are not explicitly imposed. By not restricting the boundaries in any way, the free edge boundary conditions are automatically satisfied. We do need to impose conditions to prevent rigid-body movement. Because the large deformations will occur near the edges, the center is fixed in all directions. To induce displacement in the z-direction we create an imperfection. We apply a small imperfection force to the circular plate at the start of the simulation. This force is applied to all nodes in the outer circle to preserve axisymmetry and to not produce any net moment. As for the rectangular plate, we randomize the z-coordinates of the initial position to vary slightly from the reference position. Applying a uniform force as we do for the circular plate would not break the symmetry and would not result in the wavy pattern observed in reality. During the simulation the moisture content will be raised over time. At every time step a static problem is solved using an iterative method, based on the solution of the previous step. No inertia or vibration characteristics are taken into account. Artificial damping is included to improve convergence of the nonlinear calculations.

6. Analytical and numerical results

6.1. Circular plate

To compare various results from the two approaches for the circular plate, we will initially use the following values for the relevant parameters:

- $R = 1$,
- $a = 0.1$,
- $E = 5 \cdot 10^9$,
- $\nu = 0.3$,
- $h = 0.01$ (making the thickness of the plate $2h = 0.02$),
- $\beta = 0.001$,
- $\chi = 1\%$.

For these simulations an initial 1500 elements grid will be used, the radial and tangential curves are subdivided into 30 and 50 sections respectively. Then, each element in the moistened part is subdivided into 3 elements in the radial direction, increasing the total number of elements to 1800. For these parameter values, the two in-plane stress components, given by (17) and (18) are shown in Fig. 2.

We note that the radial stress is indeed continuous and it vanishes at $r = 1$, as imposed by the boundary conditions. Apart from the difference near the center of the plate at $r = 0$, these results are similar to those obtained analytically. The discrepancy is caused by the boundary conditions imposed at the center, needed to prevent rigid-body movements in the numerical simulation, having a very local effect only.

Also the displacement in the radial direction is calculated. The comparison between the analytical solution and the numerical solution for this quantity is made in Fig. 3. An excellent agreement is observed. Also the continuity condition at $r = a$ is satisfied.

6.2. Parameters determining the buckling threshold

Now that we have briefly verified that the numerical simulation provides results similar to the analytical solution for the circular plate reference problem in the pre-buckling situation, we move on to the onset of buckling. As an illustrative example, the vertical displacement of a node at the edge of the plate resulting from the numerical simulation is shown in Fig. 4, using the parameter values given in the previous section, but for increasing χ. The buckling threshold χ_0 is clearly discernible.

In Fig. 5 we show the buckling mode, as obtained through numerical simulation.

The deflection pattern of the plate immediately after buckling can be obtained through analytical methods, but we should disregard the values on the vertical axis, since the analytical approach does not provide a unique solution for the magnitude of the dis-

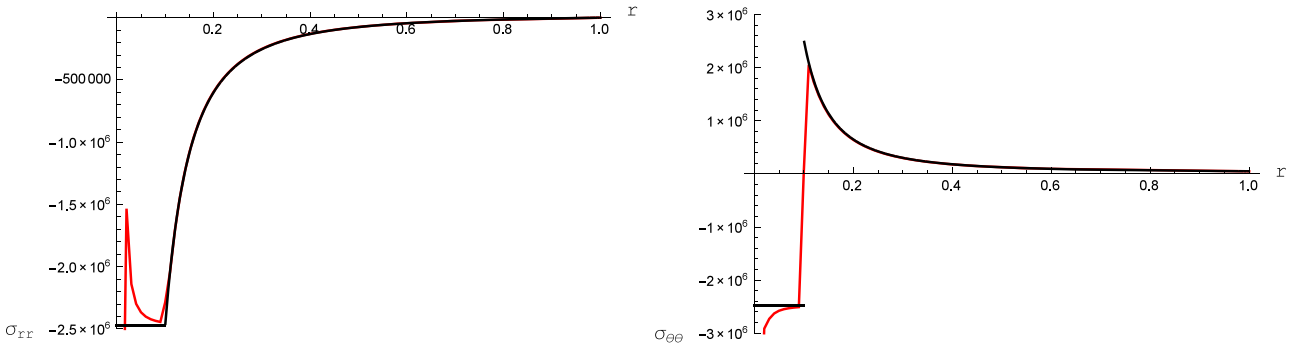

(a) Radial stress. (b) Tangential stress.

Fig. 2. Distributions of radial and tangential stress in radial direction, from the analytical method (in black) and from the numerical simulation (in red), for the parameter values given in the text. (For interpretation of the references to colour in this figure legend, the reader is referred to the web version of this article.)

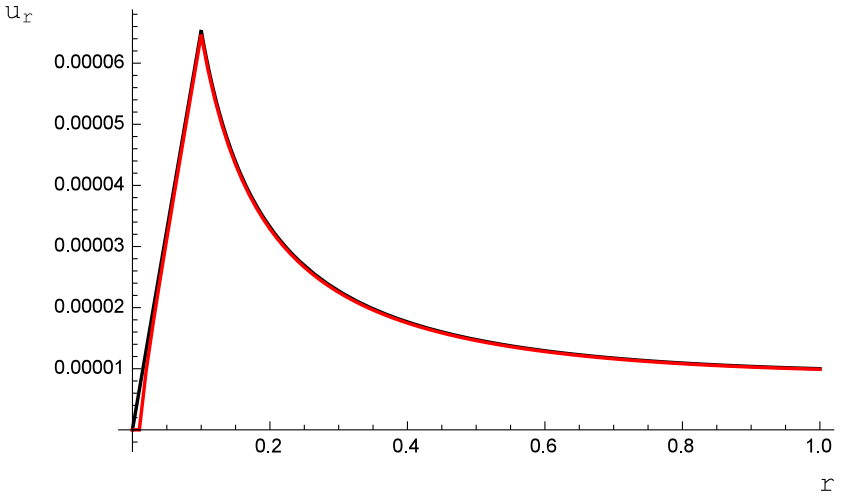

Fig. 3. Distribution of the radial displacement in radial direction, obtained from the analytical method (in black) and from the numerical simulation (in red), for the parameter values given in the text. (For interpretation of the references to colour in this figure legend, the reader is referred to the web version of this article.)

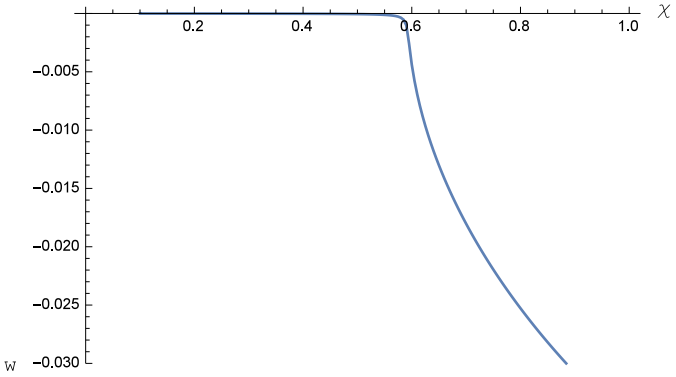

Fig. 4. Vertical displacement of a node along the edge versus the moisture content for the parameter values given in the text.

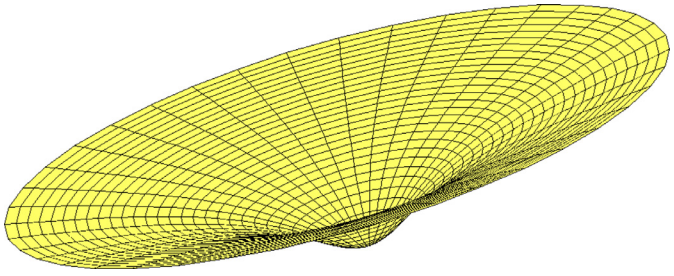

Fig. 5. The buckling mode, obtained through numerical simulation.

placement, due to nonlinearity. A good agreement in pattern is observed in Fig. 6..

Looking at the structure of system (28), we see that the dimensionless buckling parameter χ_0 depends on E, β and h only through μ. Here, we have from (12), with $\nu_{xy} = \nu_{yx} = \nu$ and $L = R$, that $\mu = 3(1-\nu^2)\beta\chi R^2/h^2$, or, in dimensional parameters,

$$\chi_0 = \left(\frac{h}{R}\right)^2 \frac{1}{3(1-\nu^2)\beta}\ \mu_0(a/R). \tag{48}$$

We note that this expression is independent of Young's modulus E and conclude that E has no influence on the buckling threshold χ_0. Physically this is evident as both the out-of-plane strain bending energy and the in-plane hygrothermal energy are proportional to E as can be seen from the corresponding expressions (41) and (43) for the rectangular plate. The effect of varying the relevant parameters individually from the previously used values should give us a first glance at the influence of each of them on the buckling threshold. The buckling threshold χ_0 is proportional to $(h/R)^2$ and inversely proportional to β and $1-\nu^2$. The effect of varying the relevant parameters from the values given in the previous section is shown in Fig. 7.

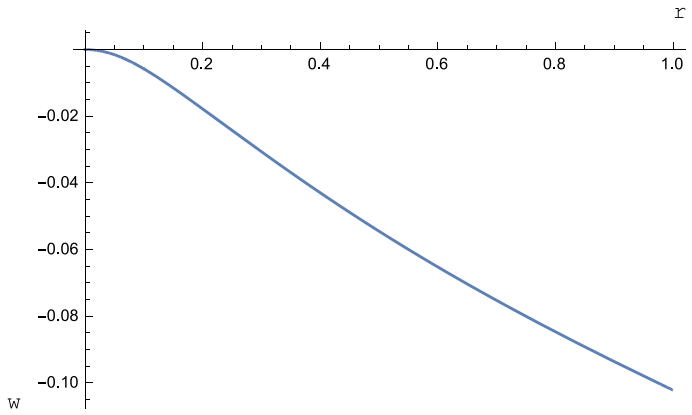

(a) Analytical solution.

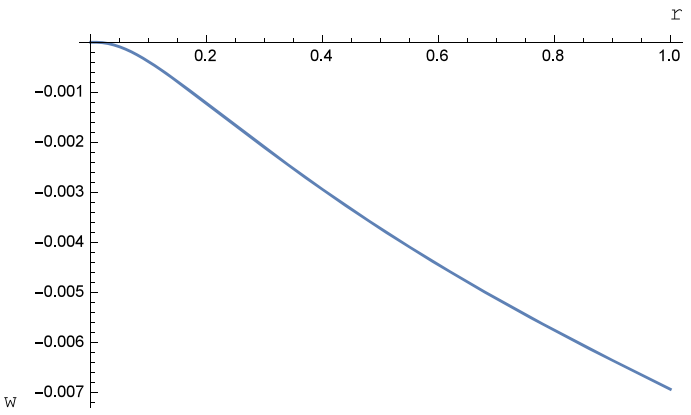

(b) Numerical simulation.

Fig. 6. Comparison of the two methods in determining the deflection pattern of the plate immediately after buckling. On the horizontal axis r is varied between the center and the edge of the plate.

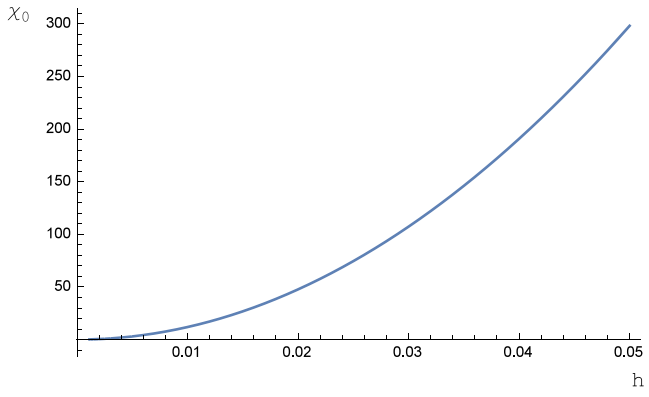

(a)

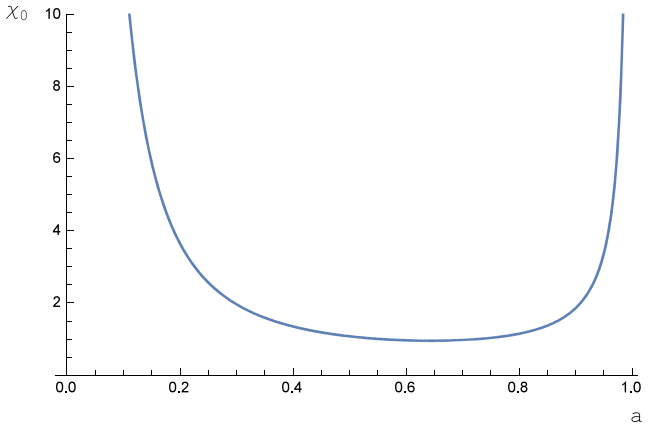

(b)

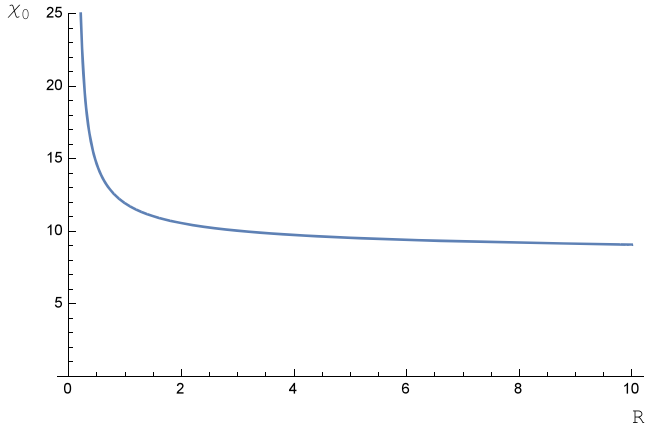

(c)

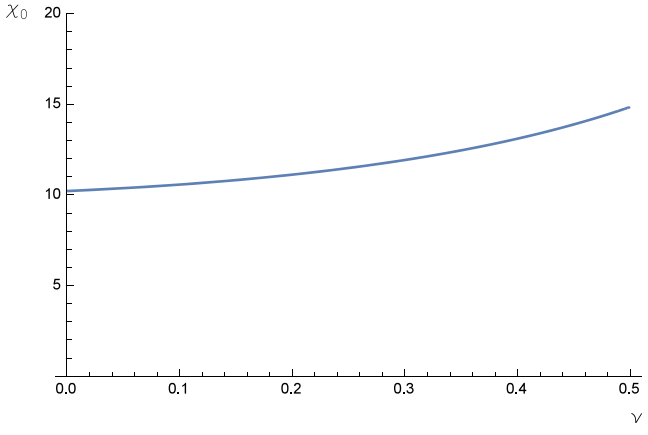

(d)

Fig. 7. Buckling threshold according to analytical approach versus (a) half of the plate thickness, (b) radius of the wet circle, (c) radius of the plate and (d) Poisson's ratio.

From physical considerations, we would expect that a plate that is not wetted ($a = 0$), or homogeneously wetted ($a = R$), will not buckle for any value of the moisture content χ. These instances appear in Fig. 7(b) as asymptotes. In Fig. 7(c) the buckling threshold converges to a certain limit as $R \to \infty$, this has been verified. This suggests that for large values of R the effect of increasing the relative size of the dry part R/a and of decreasing the relative thickness of the plate, h/R balance each other in (48).

6.3. Comparison of the analytical and numerical results

We explore the boundaries of the parameter values the numerical and the analytical method can handle, staying in accordance

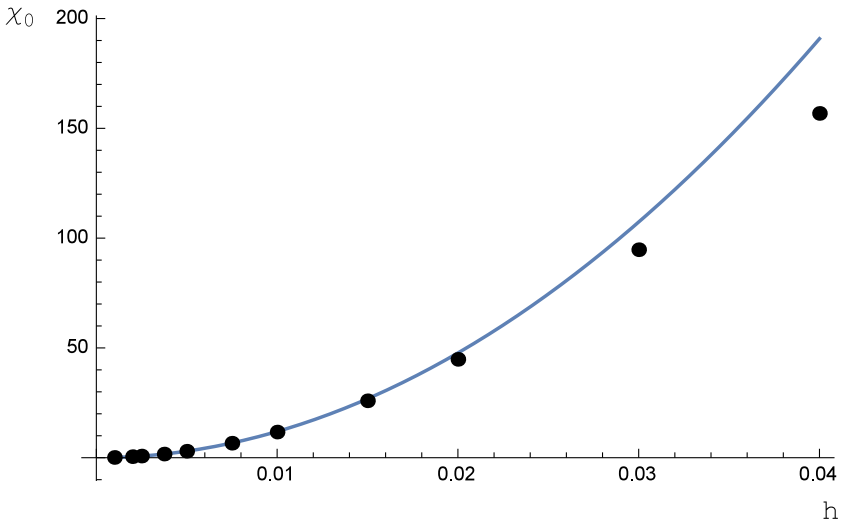

Fig. 8. Buckling threshold versus half of the plate thickness, h, numerical (black dots) and analysis (blue line). (For interpretation of the references to colour in this figure legend, the reader is referred to the web version of this article.)

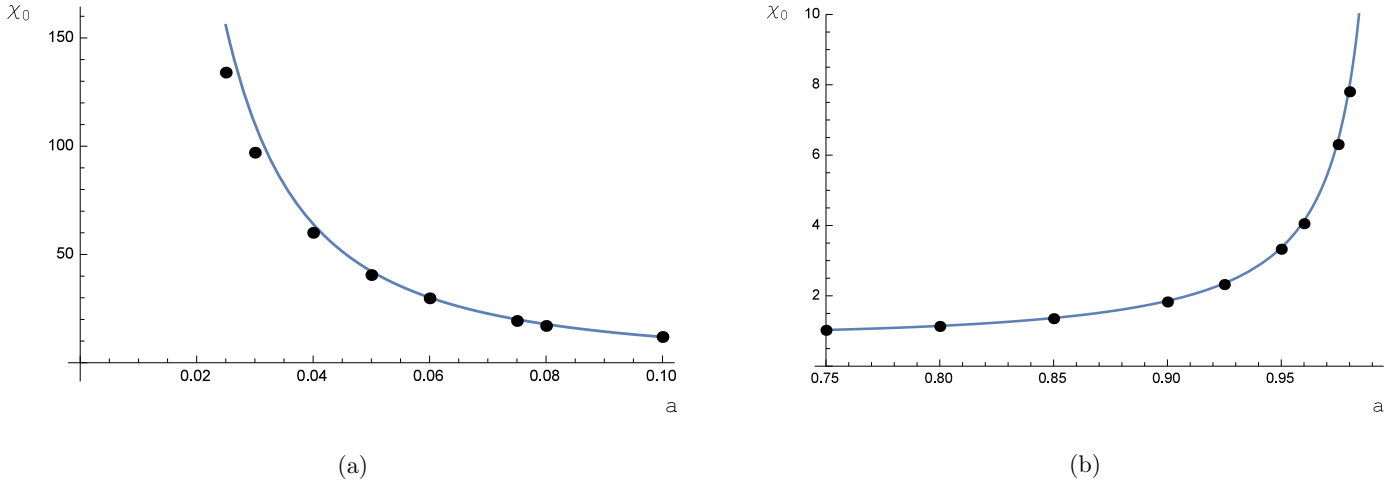

Fig. 9. Numerically (black dots) and analytically (blue line) computed buckling threshold for (a) low and (b) high values of wetted-circle radius. (For interpretation of the references to colour in this figure legend, the reader is referred to the web version of this article.)

with one another. Fig. 8 shows the dependence on h for both methods. In this and the other figures in this section, all the remaining parameter values are the same as in the beginning of this chapter. We see a good agreement for $h \leq 0.02$. The discrepancy for larger values of h is inherent to the limited validity of the von Kármán model: the thickness to radius ratio becomes more than 1/25, while we assumed that the thickness is negligible compared to the in-plane dimensions. Ventsel and Krauthammer (2001, Ch. 7.3) suggest that ratios below 0.05 should provide good results. The model is suitable to model for a paper sheet, with a thickness-to-width ratio of $\mathcal{O}(10^{-3})$.

When the wetted part of the plate becomes either large or small, this could cause problems in the numerical simulation. The high buckling threshold χ_0 causes a long running time and may induce convergence problems. Moreover it could be difficult to capture the behavior of the small region in the numerical simulation. For small values of a extra attention is paid to this in setting up the simulation, since the boundary conditions to prevent rigid-body movements are imposed at the center. A comparison between simulation and analysis for various values of a is made in Fig. 9.

The numerical results agree well with the analytical ones. The dependence of the buckling threshold on R is shown in Fig. 10. An excellent agreement is observed, even for small values of R down to twice the moistened part of the plate ($a = 0.1$).

Now that we have explored the behavior of the buckling threshold near the limits of the admissible parameter values, we will consider a range of parameter values comparable to the wetting of paper. The parameter values considered are:

- $\nu = 0.1,\ 0.4,$
- $R = 0.1,\ 1,$
- $R/a = 2,\ 20,$
- $R/h = 500,\ 5000.$

The material properties of the paper sheet in most paper wetting situations will be inside this range of values. We compare numerical simulation results to analytical results for these 16 instances. The results are given in Table 1. The results from the numerical simulation agree well with the analytically obtained values of the buckling threshold. We conclude, based on the results for this reference problem, that the numerical simulation and the analytical method agree well with each other in describing the wetting of a paper sheet up to the onset of buckling.

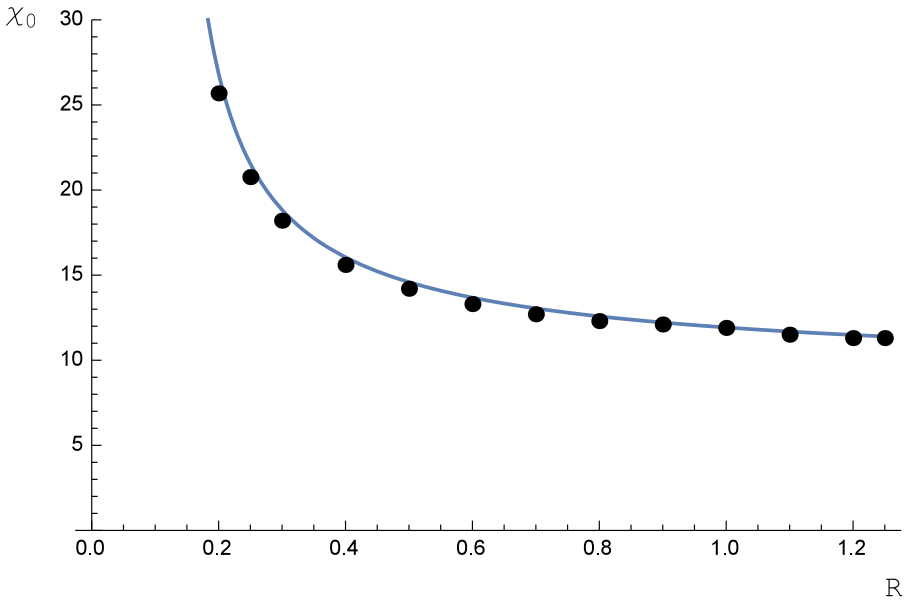

Fig. 10. Numerically (black dots) and analytically (blue line) computed buckling threshold versus plate radius. (For interpretation of the references to colour in this figure legend, the reader is referred to the web version of this article.)

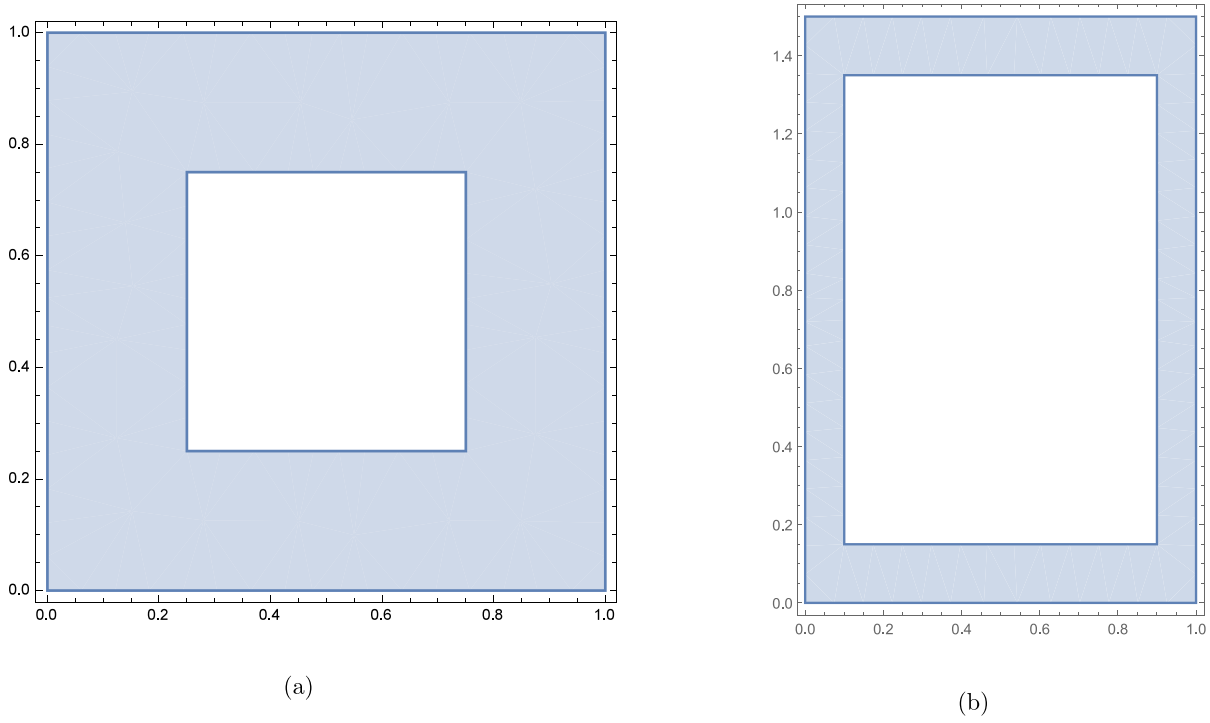

Fig. 11. The moisture distributions used for (a) plate 1, with the moisture penetrating up to 1/4th in both directions, and (b) plate 2, 3 and 4, with the moisture penetrating up to 1/10th in both directions.

6.4. Rectangular plate

To compare the results for rectangular plates obtained by numerical simulation with those obtained by the Rayleigh–Ritz method, we consider the following four reference plates:

- Plate 1: square 1 m $\times$ 1 m, isotropic plate with $E = 10^9$ Pa, $h =$ 0.0005 m and $\nu = 0.3$ exposed to the moisture profile shown in Fig. 11(a),
- Plate 2: 1 m $\times$ 1.5 m, same isotropic plate as plate 1, exposed to the moisture profile shown in Fig. 11(b),
- Plate 3: 1 m $\times$ 1.5 m orthotropic plate with $h = 0.0005$ m, $E_x = 8 \cdot 10^9$ Pa, $G_{xy} = E_y = 2 \cdot 10^9$ Pa, $\nu_{xy} = 0.3$, $\nu_{yx} = 0.075$, $\beta_y = 5\beta_x$, exposed to the moisture profile shown in Fig. 11(b),
- Plate 4: 0.2 m $\times$ 0.3 m orthotropic plate with otherwise the same parameter values as plate 3, exposed to the moisture profile shown in Fig. 11(b).

The numerical simulations are carried out using a 30×30 grid for plate 1 and a 30×45 grid for the other plates. The in-plane stress profiles of the pre-buckled plate 1 obtained by means of both methods are compared. As we can see in Figs. 12, 13 and 14, the stress profiles obtained by means of the analysis are similar to

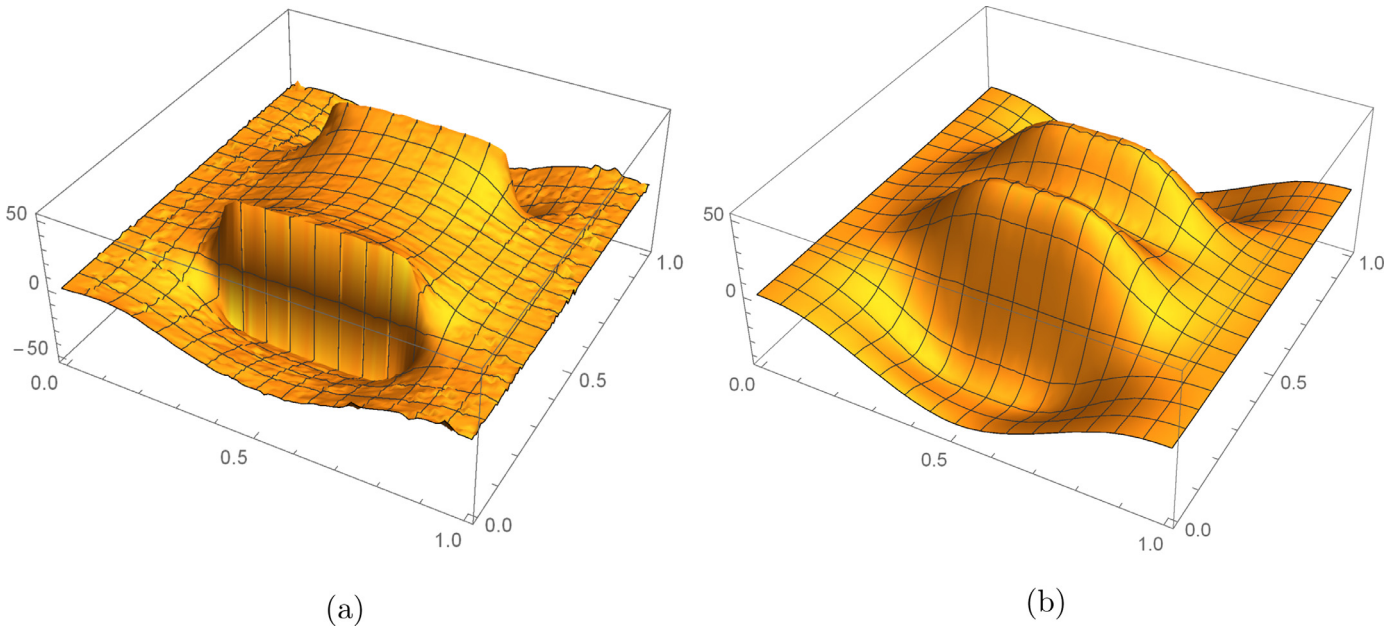

Fig. 12. Stress σ_{xx} in plate 1 obtained by (a) numerical simulation and (b) analysis.

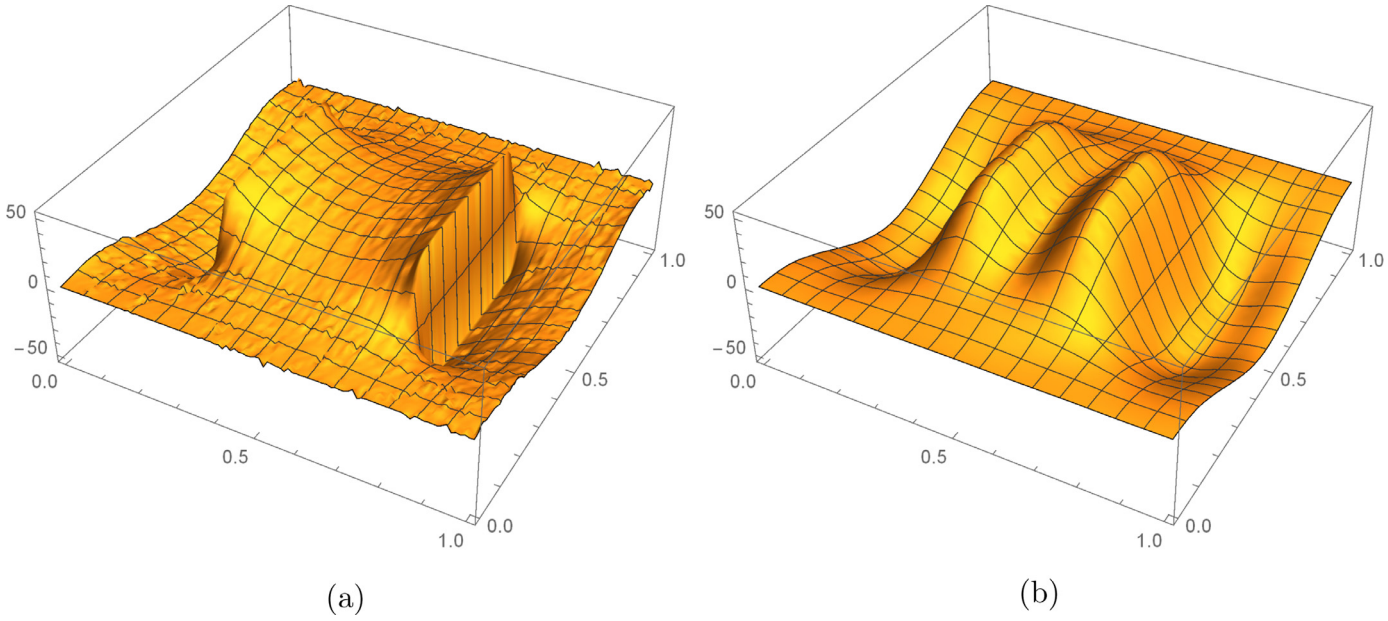

Fig. 13. Stress σ_{yy} in plate 1 obtained by (a) numerical simulation and (b) analysis.

the results of the numerical simulation. This comparison is made for the other three plates under consideration as well, also showing this resemblance. However, the numerically obtained stresses contain a discontinuity that cannot be described by the smooth functions we use in the analytical solution.

Next we use the Rayleigh–Ritz method to approximate the buckling thresholds for the plates, and compare the results to the values obtained in the numerical simulation. The Rayleigh–Ritz method is applied by approximating the clamped beam functions (33) with a Fourier series for efficiency purposes. We also make use of the symmetry in the plates to improve the computational efficiency of the numerical simulation. As coordinate functions for the deflection we use a Fourier cosine series, with the terms symmetric with respect to 1/2. Trials are executed with various amounts of terms. It shows that adding terms beyond 10 does not substantially change the results.

The Rayleigh–Ritz method is well-suited to quickly obtain an upper bound for the buckling threshold. Even a crude estimation of the deflected shape will result in a good approximation of the buckling threshold. Finding the buckling shape of the plate is a more time-consuming task with this approach. Table 2 gives the buckling threshold for the four plates.

In all four cases, the buckling threshold obtained using the Rayleigh–Ritz method is about 10% higher than the value from the numerical simulation.

Fig. 15 shows the buckling modes, corresponding to the three lowest critical moisture contents, i.e. the first three solutions to (44), for plate 3. These results have been obtained with the analytical method. The FEM-model gives similar results. We see that

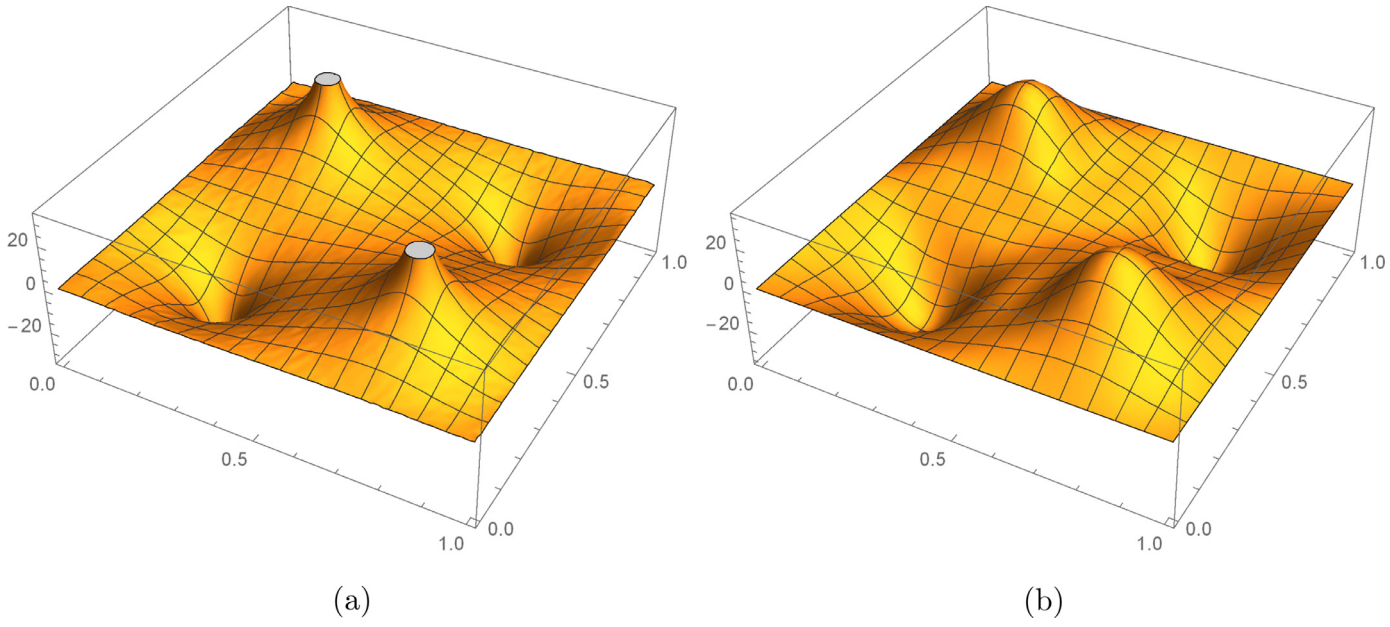

Fig. 14. Stress σ_{xy} in plate 1 obtained by (a) numerical simulation and (b) analysis.

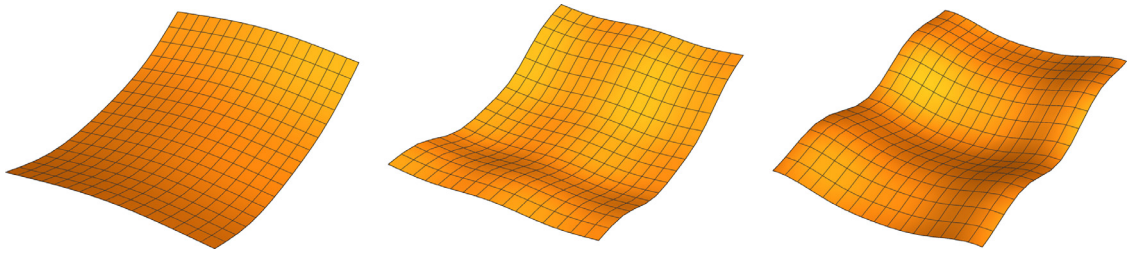

Fig. 15. The modes corresponding to the first three eigenvalues of plate 3, obtained through Rayleigh–Ritz analysis.

Table 1
Numerically (Marc Mentat) and analytically obtained buckling threshold for various relevant combinations of parameter values.

ν	R	R/h	R/a	χ_0, Marc Mentat	χ_0, Rayleigh–Ritz
0.1	0.1	500	2	0.036	0.036
			20	1.5	1.5
		5000	2	0.0021	0.0021
			20	0.015	0.015
	1	500	2	0.036	0.036
			20	1.5	1.5
		5000	2	0.00036	0.00036
			20	0.016	0.015
0.4	0.1	500	2	0.048	0.048
			20	1.8	1.8
		5000	2	0.00048	0.00048
			20	0.019	0.018
	1	500	2	0.048	0.048
			20	1.9	1.8
		5000	2	0.00048	0.00048
			20	0.019	0.018

Table 2
Analytically and numerically computed buckling thresholds for the four plates.

Plate	$\beta_x\chi$, Rayleigh–Ritz	$\beta_x\chi$, Marc Mentat
1	8.1×10^{-8}	7.5×10^{-8}
2	6.2×10^{-8}	5.6×10^{-8}
3	2.8×10^{-8}	2.6×10^{-8}
4	7.0×10^{-7}	6.4×10^{-7}

the higher the order of the modes, the more dominant the wavy pattern becomes.

7. Conclusions

The shape of paper sheets is strongly influenced by non-uniform water absorption. In this study, we specifically looked at in-plane moisture differences. When the differences in moisture content become large enough, the sheet will buckle. In the case considered here, large out-of-plane deformations occur at the edges, forming a wavy pattern and causing the paper to lose its flatness required for printing purposes.

An isotropic circular plate with a moistened center has been considered. A method to determine the stresses, the buckling threshold, and the buckling mode in terms of Bessel functions has been presented. Numerical solutions of this problem are consistent with these analytical solutions, for various values of the relevant parameters. Both solution methods show that of the parameters considered, the buckling threshold is hardly influenced by material properties, apart from the coefficient of hygro-expansion.

To approximate the buckling threshold of a rectangular orthotropic plate with moistened edges a variational method has been presented. First the stress function has been determined solving the variational form of the in-plane part of the *von Kármán equations* for the initial, flat configuration, and from this the in-plane stresses have been found. A numerical method applied to this problem has shown to provide similar results for these stresses. Next this stress function has been incorporated in a Rayleigh–Ritz method to approximate the buckling threshold. The

buckling threshold has been calculated for four reference plates by both methods. This showed that the numerical simulation is consistent with the Rayleigh–Ritz method. Both buckling values for all four cases are of the same order of magnitude, certainly within the accuracy expected in industrial applications. Moreover, the Rayleigh–Ritz values are all somewhat higher than the numerical ones. This is to be expected, since, as discussed in Section 4.2, the Rayleigh–Ritz method always gives an overestimate for the buckling value. The analytical and numerical methods are consistent with one another.

Acknowledgment

This work was conducted at the research and development facility of Océ, in Venlo, the Netherlands. The support by Océ is highly appreciated.

References

Abramowitz, M., Stegun, I.A., 1972. Handbook of Mathematical Functions. United States Department of Commerce.
Audoly, B., Boudaoud, A., 2003. Self-similar structures near boundaries in strained systems. Phys. Rev. Lett. 91, 086105.
Chester, S., Anand, L., 2011. A thermo-mechanically theory for fluid permeation is elastomeric material: application to thermally responsive gels. J. Mech. Phys. Solids 59, 1978–2006.
Dervaux, J., Ciarletta, P., Amar, M.B., 2009. Morphogenesis of thin hyperelastic plates: a constitutive theory of biological growth in the Föppl-von Kármán limit. J. Mech. Phys. Solids 57, 458–471.
Efrati, E., Sharon, E., Kupferman, R., 2009. Elastic theory of unconstrained non-Euclidian plates. J. Mech. Phys. Solids 57, 762–775.
Giannopoulos, G., Santafe, F., Monreal, J., Vantomme, J., 2007. Thermal, electrical, mechanical coupled mechanics for initial buckling analysis of smart plates and beams using discrete layer kinematics. Int. J. Solids Struct. 44, 4707–4722.
Goldmann, G., Michel, L., 2001. The World of Printers, Technologies of Océ Printing Systems. Chapter 6: Paper is a living material. Océ, Venlo, The Netherlands.
Gossard, M., Seide, P., Roberts, W., 1952. Thermal Buckling of Plates. NACA TND, USA, p. 2771.
Hetnarski, R.B., 2013. Encyclopedia of Thermal Stresses. Springer.
Klein, Y., Efrati, E., Sharon, E., 2007. Shaping of elastic sheets by prescription of non-Euclidian metrics. Science 315, 1116–1120.
Lekhnitskii, S.G., 1957. Anisotropic Plates, Translation by USA Foreign Technology Division. Pennsylvania State University.
Leppänen, T., 2007. Effect of Fiber Orientation on Cockling of Paper, Doctoral thesis. University of Kuopio.
Liang, H., Mahadevan, L., 2009. The shape of a long leaf. PNAS 106 (52), 22049–22054.
Lipponen, P., Leppänen, T., Kouko, J., Hämäläinen, J., 2008. Elasto-plastic approach for paper cockling phenomenon: on the importance of moisture gradient. Int. J. Solids Struct. 45, 3596–3609.
Ma, L., Wang, T., 2003. Nonlinear bending and post-buckling of a functionally graded circular plate under mechanical and thermal loadings. Int. J. Solids Struct. 40, 3311–3330.
Marc Mentat version 2014.0.0 Beta, MSC Software. 2014.
Marin Zapata, P. A., 2010. Modeling and Computation of Heat and Moisture Transport in Paper, Master thesis. Eindhoven University of Technology.
Mead, D.J., 2003. Vibration and buckling of flat free–free plates under non-uniform in-plane thermal stresses. J. Sound Vib. 260, 141–165.
Moon, F.C., Pao, Y.H., 1968. Magnetoelastic buckling of a thin plate. J. Appl. Mech. 35 (1), 53–58.
Niskanen, K., 2012. Mechanics of Paper Products. De Gruyter.
Sharon, E., Efrati, E., 2010. The mechanics of non-Euclidian plates. Soft Matter 6, 5693–5704.
van de Ven, A.A.F., 1978. Magnetoelastic buckling of thin plates in a uniform transverse magnetic field. J. Elast. 8, 297–312.
Ventsel, E., Krauthammer, T., 2001. Thin Plates and Shells, Theory Analysis and Applications. Marcel Dekker Inc.